Desalination and Water Treatment
www.deswater.com
doi: 10.1080/19443994.2014.912158

55 (2015) 39–52
June

Taylor & Francis
Taylor & Francis Group

Analysis of heat and mass transfer in vacuum membrane distillation for water desalination using computational fluid dynamics (CFD)

Hossein Hayer, Omid Bakhtiari, Toraj Mohammadi*

Faculty of Chemical Engineering, Research Center for Membrane Separation Processes, Iran University of Science and Technology (IUST), Narmak, Tehran, Iran, Tel. +00 98 21 77240496; Fax: +00 98 21 77240495; email: torajmohammadi@iust.ac.ir

Received 27 October 2013; Accepted 29 March 2014

ABSTRACT

Water shortage is a serious problem worldwide and will be even more critical in the next decades. Vacuum membrane distillation (VMD) is a separation process which has been widely studied for water desalination. The main merit of VMD over common thermal processes is its applicability in sub-boiling feed temperatures. A robust mathematical model can evaluate potentials of VMD industrial applications. A comprehensive model was developed in this study to investigate different VMD parameters in hollow fiber membrane modules. Due to its complexity, a numerical approach was considered for building the model. COMSOL multi-physics, which is a software package based on finite element method, was applied as the solver. A combination of Knudsen, free diffusion, and viscous flow were applied to obtain flow distribution in the membrane. Two vapor pressure models, the ideal solution model and the empirical model were applied to calculate vapor pressure. The effect of each model in evaluating transmembrane flux was investigated. Maximum error for empirical vapor pressure- based model was less than 15%. It was observed that at high temperature and for high concentration, ideal solution model exhibits significant deviation from the experimental results. The effect of concentration polarization on transmembrane flux was also investigated.

Keywords: Heat and mass transfer; Vacuum membrane distillation; Water desalination; Computational fluid dynamics

1. Introduction

The demand for good-quality drinking water is steadily increasing due to population growth, economic development, rapid urbanization, and large-scale industrialization [1,2]. It is predicted that 60% of the earth's population is expected to suffer from serious water shortages by 2025 [3]. To solve these problems, desalination processes have received great attention as alternative methods for freshwater production from contaminated waters [4]. Application of renewable energy for desalination is a green solution for the problem of reliable water resources [5,6].

Membrane distillation (MD) is a suitable separation technology used for aqueous solutions which utilizes porous hydrophobic membranes in a non-isothermal process which is driven by vapor pressure differences across the membrane [7–9]. The membrane just acts as a physical support for the vapor–liquid interface located at the pore entrance [10]. The main application of the MD is the treatment of brackish seawater or

*Corresponding author.

high salinity water in order to produce ultrapure water [11]. MD was initially introduced as a concept for seawater desalination in the 1960s, however, due to its low permeation flux compared to conventional techniques and problem of membrane wetting during operation it has not drawn much attention for decades [12]. Therefore, no industrial scale MD plant has been implemented yet for desalination [13] and only a few pilot plants have been built across the world [14]. The driving force in MD is the vapor pressure difference between the two sides of the membrane and can be provided by different possibilities [15]; direct contact membrane distillation (DCMD) [11,16,17], air gap membrane distillation [18], vacuum membrane distillation (VMD) [19,20], and sweeping gas membrane distillation [21]. In comparison with other desalination methods, MD has several advantages such as 100% rejection of non-volatile components, low operating pressure that is not altered by feed concentration as is the case for reverse osmosis, non-complex construction and operation, small vapor space conventional distillation processes, and low operating temperatures which can utilize low-grade waste and/or alternative energy sources such as solar [15,22].

In VMD, the downstream pressure is kept below the corresponding feed vapor pressure by means of a vacuum pump [10,23]. The permeated vapor is then condensed in a downstream chamber [23]. By reducing vacuum downstream pressure, higher transmembrane fluxes can be achieved even at lower feed temperatures [10]. This can be considered as a potential for VMD to be applied for enrichment of temperature-sensitive solutions [24]. Several researchers have tried to model this process; Soni et al. [24] used universal quasi-chemical functional group activity coefficients (UNIFAC) to calculate interfacial vapor pressures in flat sheet modules used for the separation of aromatic compounds. Diban et al. [25] also used UNIFAC. They considered the effects of both free and Knudsen diffusion in membrane transport. Zhang et al. [23] took effect of Poiseuille flow into account and used their modeling procedure as a tool to determine membrane properties. In all mentioned works, effects of concentration and temperature polarization were not considered and heat and mass transfer coefficients in feed side were calculated from empirical correlations.

Combination of all transport phenomena in the MD model makes it complex. Reasonable understanding of fluid dynamics, heat and mass transfer mechanisms in industrial membrane separation processes is crucial for proper apparatus design and optimization of operating conditions [26]. An alternative modeling approach involves computational fluid dynamic (CFD) simulations [27]. CFD is a powerful tool for modeling systems involving fluid flow, heat transfer, mass transfer, and associated phenomena using computer numerical simulation and is being increasingly applied in the membrane field [28,29]. Since the late 1990s, CFD has been used as a modeling technique for modeling complex geometries in steady or unsteady state modes. Utilizing this technique, polarization effect can be comprehensively investigated [30]. CFD packages are mainly based on control volume methodology, local variations of fluid, thermal, and mass transport properties can be visualized in comparison to simple models [31]. One of the most applied commercial softwares used in CFD computations is the FLUENT [32]. Some researchers [33,34] considered membrane to be impermeable; based on this assumption and considering negligible heat consumption or generation due to water evaporation or condensation, they obtained heat transfer coefficient in spacer-enhanced modules. Some others [35,36] developed models to simulate heat and mass transfer coefficients in the modules. They first calculated velocity and temperature distributions in modules, next they obtained mass flux- based available temperatures, therefore effect of mass transfer on heat and momentum transfer was ignored. Tang et al. [37] used Darcy's model to obtain mass transfer in membrane used for VMD; their model poorly predicted the experimental data. Ghadiri et al. [38] presented a comprehensive two-dimensional model and considered different transport phenomena for DCMD in a flat sheet membrane module, however, the effect of concentration polarization was not considered in their model. They used COMSOL as a finite element-based software package, to apply complicated equations to their model.

Due to lack of published works regarding mathematical modeling of VMD, development of a reliable mathematical model is necessary to further study the separation process via VMD fundamentally. The current study presents a new comprehensive model based on CFD concepts to investigate VMD in hollow-fiber membrane modules. Fluid mechanics, heat and mass transfer are considered along the membrane module. Modeling of surficial evaporation requires precise knowledge of mixture thermodynamics. Two applied thermodynamic models, ideal mixture model and empirical model are employed to study the effect of vapor pressure on the feed membrane surface. The effect of evaporation on feed side fluid dynamics is also studied to give a clear picture of concentration polarization. Temperature polarization is also an important phenomenon in MD and it cannot be directly evaluated by the experiment. The aim of this work is to study the effects of different parameters on

transmembrane flux and temperature polarization coefficient.

2. Methodology

The experimental data reported by Fang et al. [39] for VMD were used to validate this simulation. In the experiments, hot feed solution was circulated through the shell side of a hollow-fiber module and make-up heat and water were provided outside the module. Permeated vapor was being condensed via an external condenser and collected in a tank. Desired vacuum level was provided and controlled by a downstream vacuum pump. The experimental operating conditions are summarized in Table 1.

A comprehensive two-dimensional axisymmetric model is used to simulate momentum, heat and mass transfer in VMD. Since the membrane is hydrophobic, it is assumed that no water droplet enters the membrane pores, and a non-wetted approach is assumed for numerical simulation for the hollow-fiber module. Vapor and liquid in both membrane–feed and membrane–permeate interfaces are assumed to be in thermodynamic equilibrium.

The model was based on the following assumptions:

(1) Steady-state condition.
(2) Membrane is fully hydrophobic and no water enters through the membrane pores.
(3) No solute (salt) is transferred and 100% rejection is achieved.
(4) No slip condition at the membrane surface.

It should be noted when the vacuum pressure gets lower than a certain level (breakthrough pressure), pore wetting occurs and the second assumption is no longer valid. The steady-state assumption is not also valid at the start-up transient time of the experimental setup. Based on the experimental setup which was used by Fang et al. [39], the applied assumptions could be considered valid.

Table 1
Operating conditions [39]

Condition	Value
Vacuum pressure (bar)	0.04–0.25 bar
Feed flow rate (Lit/min)	20
Fiber length (cm)	10
Membrane porosity (%)	42.8
Membrane pore size (μm)	0.7
Solution concentration (%)	2–6 wt
Inlet temperature (°C)	50–80
Membrane thickness (mm)	0.2
Inner diameter (mm)	1.4

2.1. Model equations

Numerical modeling in three-dimensional mode is a time-consuming task and it is considered to be a computational expensive problem. In order to reduce the three-dimensional space to two-dimensional space, a unit simulation cell for a typical membrane fiber must be considered (Fig. 1). The hollow-fiber module consisted of a bundle of fibers in a shell. In order to study the hollow-fiber module, it is not necessary to study the whole system. The results of studying a single fiber can be extended to the whole module. In two-dimensional axisymmetric approach, a simulation cell consists of three rectangles; one for feed domain, another for membrane domain, and the other for permeate domain (Fig. 2). Happel's free surface model [40] is applied to estimate the shell side radius. The radius of free surface ($r3$ in Fig. 2) is defined as (Eq. (1)):

$$r3 = \left(\frac{1}{1-\phi}\right)^{1/2} r2 \tag{1}$$

In which ϕ is volume fraction of void and $r2$ is outer radius of a single fiber.

2.1.1. Momentum transfer in lumen and sell sides

Momentum transfer in shell and lumen sides is evaluated by simultaneously solving continuity (Eq. (2)) and Navier–Stokes equations (Eq. (3)):

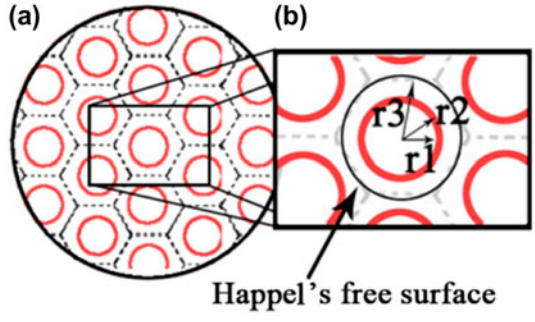

Fig. 1. (a) A typical hollow-fiber membrane module (cross-view) and (b) geometry nomenclature.

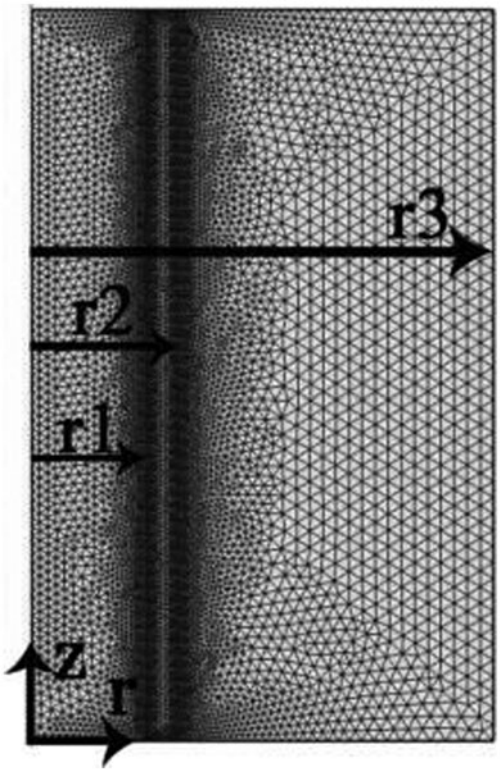

Fig. 2. Triangular mesh grid used in the present simulation.

$$\nabla \cdot (\rho u) = 0 \tag{2}$$

$$\rho(u \cdot \nabla)u = \nabla \cdot (-p + \mu(\nabla u)) \tag{3}$$

In which ρ, u, p, and μ represent density (kg/m^3), velocity vector (m/s), pressure (Pa), and dynamic viscosity (Pa s), respectively.

In this study, effects of transmembrane flux on shell and lumen hydrodynamics are considered. Both contributions of diffusive and convective flux are also considered. Outlet velocity from shell side to membrane is calculated as (Eq. (4)):

$$u = \frac{\left(\partial C^{mem.}_{vapor}/\partial r\right) D_{eff} M_w}{\rho_w} - u^{mem.}_{r,darcy} \frac{\rho_v}{\rho_w} \tag{4}$$

and inlet velocity from membrane to lumen side is calculated as (Eq. (5)):

$$u = \frac{(\partial C^{mem.}_{vapor}/\partial r) D_{eff} M_w}{\rho_v} - u^{mem.}_{r,darcy} \tag{5}$$

The above equation is derived by applying mass balance law. Details of boundary conditions for each domain are presented in Tables 2–4. More details on shell and lumen boundary conditions are reported in Tables 2 and 4, respectively.

Table 2
Boundary conditions in lumen side

Position	Type	Equation
Momentum transfer		
$z = 0$	Pressure	$p = p_{vac}$
$z = L$	No slip condition	$U = 0$
$r = 0$	Symmetry	$\partial U_r/\partial r = 0$
$r = r1$	Inlet velocity	Eq. (5)
Heat transfer		
$z = 0$	Convective outflow	$k\nabla T = 0$
$z = L$	Insulation	$\partial T/\partial z = 0$
$r = 0$	Symmetry	$\partial T/\partial r = 0$
$r = r1$	Temperature	$T = T_{mem.}$

2.1.2. Mass transfer in membrane

In this work, both contributions of convective and diffusive flow on transmembrane mass transfer are considered. The resistance imposed by the membrane structure can be described by either Knudsen diffusion model or Poiseuille (vicous) flow model [41]. Electrical analogy circuit of different transport mechanisms is presented in Fig. 3.

2.1.2.1. Diffusive flow. As illustrated in Fig. 3, diffusive flux depends on Fick's diffusion (Eq. (6)) and Knudsen diffusion mechanisms. It is assumed that no air molecule is present in the membrane pores; therefore ordinary diffusion coefficient used in this study is self-diffusion coefficient and is defined as [42]:

$$D_v = \frac{\mu_v}{\rho_v} \tag{6}$$

In which, D_v, μ_v, and ρ_v are self-diffusion coefficient (m^2/s), viscosity (Pa s), and density (kg/m^3) of water

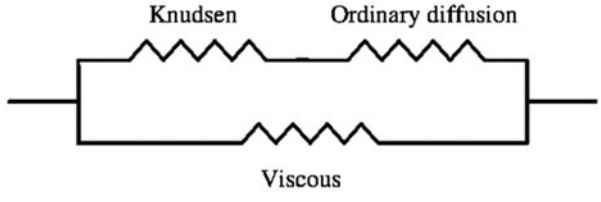

Fig. 3. Electrical analogy circuit for different mass transfer resistances.

vapor, respectively. Knudsen diffusion coefficient takes effect of membrane–wall interaction into account and is defined as follows (Eq. (7)) [43]:

$$D_{knd} = \frac{2}{3} d_p \sqrt{\frac{2RT}{\pi M_v}} \tag{7}$$

In which, d_p, R, π, M_v , and T are pore diameter (m), universal gas constant ((Pa m^3)/(mol K)), π number (dimensionless), vapor molecular weight (kg/mol), and temperature (K), respectively. The diffusion coefficients are then modified in a way that the membrane structure properties are considered as in Eqs. ((8) and (9)):

$$D_{v,eff} = \frac{\varepsilon D_v}{\tau} \tag{8}$$

$$D_{knd,eff} = \frac{\varepsilon D_{knd}}{\tau} \tag{9}$$

In which ε and τ are membrane porosity and tortuosity, respectively. The effective diffusion coefficient (D_{eff}) can be obtained using Bonsaquet Eq. (10) [44]:

$$\frac{1}{D_{eff}} = \frac{1}{D_{v,eff}} + \frac{1}{D_{knd,eff}} \tag{10}$$

In this step, it is considered that no convective flux is present in the diffusion mechanism; therefore, a simplified mass transfer Eq. (11) is used to describe diffusive flux in membrane.

$$\nabla \cdot (D_{eff} \nabla C_v) = 0 \tag{11}$$

In which C_v is molar concentration of vapor in membrane (mol/m^3).

2.1.2.2. Viscous flow. Darcy's law (Eq. (12)) and continuity Eq. (13) are used to describe viscous flow in membrane.

$$\nabla \cdot (\rho_v u) = 0 \tag{12}$$

$$u = -\frac{\kappa}{\mu_v} \nabla p \tag{13}$$

In which κ is membrane permeability (m^2) and μ is vapor viscosity (Pa s). Poiseuille's law is used to evaluate Darcy's permeability. In Poiseuille's law approach, it is assumed that the membrane consists of several channels and the fluid flow in these channels is laminar [45]. Volumetric flux in this approach is calculated as [45]:

$$u = -\frac{\Delta p\, \varepsilon}{32 \mu l\, \tau} d_p^2 \tag{14}$$

In which l is membrane thickness (m) and τ is membrane tortuosity (dimensionless). Comparing Eqs. (13) and (14):

$$\kappa = \frac{\varepsilon \cdot d_p^2}{32\, \tau} \tag{15}$$

2.1.3. Thermodynamics

In this simulation, two approaches to calculate the water interfacial vapor pressure are implemented; first, the ideal solution approach based on Raoult's law; and second, the empirical approach based on Sparrow's Eq. (20) [46].

In ideal solution approach vapor pressure is calculated by (Eq. (16)):

$$P_{\text{sat}} = x_w P_{\text{sat, pure}} \tag{16}$$

In which P_{sat} is the partial pressure of impure water (Pa) at feed–membrane interface, x_w is mole fraction of water, and $P_{\text{sat,pure}}$ is saturation partial pressure of pure water (Pa).

The saturation pressure of pure water is calculated by Antoine's law [47,48]:

$$P_{\text{sat,pure}} = 1000e^{\left(16.3872 - \frac{3885.2}{T - 42.96}\right)} \tag{17}$$

In which T is temperature at interface (K), which is obtained by Eq. (22). By dissolving each mole of NaCl, two moles of ions are liberated, thus Eq. (18) can be used to calculate water mole fraction in solution.

$$x_w = 1 - 2x_{\text{NaCl}} \tag{18}$$

where x_{NaCl} is the mole fraction of NaCl in solution. Mass balance equation is used to develop Eq. (19) that evaluates mole faction of NaCl as a function of molar concentration of NaCl.

$$x_{\text{NaCl}} = \frac{C_{\text{NaCl}} M_{\text{NaCl}}/\rho_{\text{NaCl}}}{1 - (M_{\text{NaCl}}/\rho_{\text{NaCl}} - M_w/\rho_w) C_{\text{NaCl}}} \tag{19}$$

In which C_{NaCl} , M_{NaCl}, ρ_{NaCl}, $M_{w,}$ and ρ_w are molar concentration of NaCl (mol/m^3), molecular weight of NaCl (g/mol), density of solid NaCl (g/m^3), molecular weight of water (g/mol), and density of pure water (g/m^3), respectively.

In the second approach, Sparrow's equation (Eq. (20)) was used to calculate the interfacial pressure [46]:

$$P = A + B \cdot T + C \cdot T^2 + D \cdot T^3 + E \cdot T^4 \tag{20}$$

In which A–D are composition dependent parameters which are defined as:

$$\mathrm{A} = (0.9083 - 0.569w_{\mathrm{NaCl}} + 0.1945w_{\mathrm{NaCl}}^2 - 3.736w_{\mathrm{NaCl}}^3 + 2.82w_{\mathrm{NaCl}}^4) \times 10^{-3} \tag{20.a}$$

$$\mathrm{B} = (-0.0669 + 0.0582w\mathrm{NaCl} - 0.1668w_{\mathrm{NaCl}}^2 + 0.676w_{\mathrm{NaCl}}^3 - 2.09w_{\mathrm{NaCl}}^4) \times 10^{-3} \tag{20.b}$$

$$\mathrm{C} = (7.541 - 5.143w_{\mathrm{NaCl}} + 6.482w_{\mathrm{NaCl}}^2 - 52.62w_{\mathrm{NaCl}}^3 + 115.7w_{\mathrm{NaCl}}^4) \times 10^{-6} \tag{20.c}$$

$$\mathrm{D} = (-0.0922 + 0.0649w_{\mathrm{NaCl}} - 0.131w_{\mathrm{NaCl}}^2 + 0.802w_{\mathrm{NaCl}}^3 - 1.986w_{\mathrm{NaCl}}^4) \times 10^{-6} \tag{20.d}$$

$$E = (1.237 - 0.753w_{\mathrm{NaCl}} + 0.1448w_{\mathrm{NaCl}}^2 - 6.964w_{\mathrm{NaCl}}^3 + 14.61w_{\mathrm{NaCl}}^4) \times 10^{-9} \tag{20.e}$$

In which w_{NaCl} is the mass fraction of NaCl in shell side water. Using other empirical vapor pressure equations instead of Eqs. (16)–(20), this model can be modified for other solutions rather than the NaCl solution.

2.1.4. Mass transfer in shell

Solute concentration has a significant effect on process performance, especially at high concentrations. By calculation of an accurate solute concentration distribution in feed domain, the model reliability can be increased. Both convective and diffusive transport mechanisms are considered for evaluating NaCl concentration in shell side. Convective and diffusive mass transfer mechanisms for NaCl are considered in Eq. (21):

$$\nabla(-D_{\mathrm{NaCl-water}}\nabla C_{NaCl}) + u \cdot \nabla C_{\mathrm{NaCl}} = 0 \tag{21}$$

In which $D_{\mathrm{NaCl\text{-}water}}$, $C_{\mathrm{NaCl,}}$ and u are NaCl-water diffusion coefficient, molar concentration of NaCl, and velocity vector, respectively. Required boundary conditions for solving these PDEs are summarized in Tables 4. Velocity in Eq. (21) is substituted by velocity obtained in solving Eq. (3).

2.1.5. Heat transfer in module

MD is a thermally driven process and thus an accurate evaluation of temperature is necessary. Using energy balance equation in shell and lumen sides, a PDE based on convective and conductive heat transfer is derived for shell and lumen sides (Eq. (22)):

$$\rho_w C_{p,w} u \cdot \nabla T = \nabla \cdot (k_w \nabla T) \tag{22}$$

In which ρ_w, $C_{p,}$ and k are density (kg/m^3), specific heat capacity (J/(kg K)), and thermal conductivity (W/m.K), respectively. Since solute concentration is low, all heat transfer parameters are set based on pure water properties. Velocity vector in Eq. (22) is calculated by Eq. (3). Convective heat transfer is neglected in membrane. Therefore, Eq. (23) is used to describe heat transfer in membrane:

$$\nabla \cdot (k_m \nabla T) = 0 \tag{23}$$

In which k_m is membrane thermal conductivity which is the average thermal conductivity of membrane polymer material and flowing vapor (Eq. (24)):

$$k_m = \varepsilon k_v + (1 - \varepsilon) k_{pol.} \tag{24}$$

In which k_v and k_p are vapor thermal conductivity (W/m K) and polymer thermal conductivity (W/m K), respectively. Evaporation of water on membrane–feed interface causes heat consumption on membrane–feed boundary. Combining heat and mass conservation laws leads to Eq. (25) which is used to evaluate total heat per unit area of membrane:

$$\text{Boudary heat flux} = (\partial C_v/\partial r) D_{eff} M_w L_w - u_{darcy} \rho_v L_w \tag{25}$$

where Mw, Lw, and u_{darcy} are molecular weight of water (kg/kmol), enthalpy of vaporization (kJ/kg), and velocity obtained by Darcy's law (m/s), respectively. Since lumen side is always considered to be pure, only momentum and heat transfer governing

PDEs are solved for lumen side as presented in Table 2.

Since in dusty gas model, separate PDEs are devoted to describe viscous and diffusive flows in membrane, two sets of boundary conditions are needed to solve corresponding equations. Proposed boundary conditions for solving these equations are summarized in Table 3.

In shell side, like membrane, all transport phenomena are considered, however, mass transfer equation is used to obtain NaCl concentration instead of vapor concentration. Governing boundary conditions for solving the above mentioned properties are summarized in Table 4.

2.2. Numerical algorithm

Commercial software COMSOL is used to solve the involving non-linear PDEs in the present modeling task. Discretization and numerical solving algorithms are based on finite element method. Totally, 19,707 elements are created, in which, 19,183 were triangular, 524 were quadrilateral, 807 are edge and eight are vertex elements. Since the problem involves solving several non-linear dependent PDEs, a carefully determined initial guess should be used. Preparation algorithm of this initial guess is as follows:

(1) Take parameter values for a moderate process condition, build the geometry of three domains (lumen, membrane, and shell) and design a proper mesh.
(2) Consider membrane to be impermeable and all domains isothermal. Solve Navier–Stokes equations to obtain velocity field in shell side.

Table 3
Boundary conditions in membrane

Position	Type	Equation
Mass transfer		
$z = 0$ and $z = L$	Insulation	$J_v = 0$
$r = r1$	Concentration	$P_{lum.}/(RT)$
$r = r2$	Concentration	$P_{sat}/(RT)$
Momentum transfer		
$z = 0$ and $z = L$	Insulation	$\partial U_Z/\partial z = 0$
$r = r1$	Pressure	$P_{lum.}$
$r = r2$	Pressure	P_{sat}
Heat transfer		
$z = 0$ and $z = L$	Insulation	$\partial T/\partial z = 0$
$r = r1$	Temperature	$T = T_{lum.}$
$r = r2$	Boundary heat source	Eq. (25)

Table 4
Boundary conditions in shell side

Position	Type	Equation
Momentum transfer		
$z = 0$	Inlet velocity	$U = U_{0,F}$
$z = L$	Pressure	$p = 0$
$r = r2$	Outlet velocity	Eq. (4)
$r = r3$	Open boundary	$\nabla U = 0$
Heat transfer		
$z = 0$	Constant temperature	$T = T_{0,F}$
$z = L$	Outflow	$.k\nabla T = 0$
$r = r2$	Boundary heat source	Eq. (25)
$r = r3$	Symmetry	$\partial T/\partial r = 0$
Mass transfer		
$z = 0$	Constant concentration	$C = C_{0,feed}$
$z = L$	Outflow	$D_s\nabla C = 0$
$r = r2$	Insulation	$N_s = 0$
$r = r3$	Symmetry	$N_s = 0$

(3) Use the results obtained in step 2 as initial guess, consider the permeability of membrane and solve the momentum and mass transfer equations in membrane.
(4) Use the results obtained in step 3 as initial guess and obtain the temperature.
(5) Use the results obtained in step 4 as initial guess, solve the model considering all involved equations and save the result as initial guess for further calculation.

Flow chart of described algorithm for preparation of feasible initial guess is schematically described in Fig. 4.

Once a reliable comprehensive initial guess is ready, other operating conditions can be solved based on the initial guess proposed by the first procedure (Fig. 4) which is illustrated in Fig. 5. Instigating the effect of different operating conditions and visualizing important parameters such as velocity, temperature, or concentration is known as post processing step, which will be discussed in the next section. Constructing a reliable initial guess not only makes the solving process to be possible in extreme conditions, but also speeds up convergence of the procedure in every condition.

3. Results and discussion

Mean vapor flux on shell–membrane interface is the main parameter that is used to study the process behavior. Contributions of both conductive and

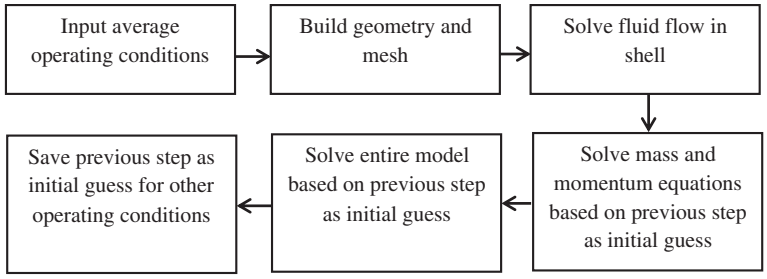

Fig. 4. Algorithm of evaluating initial guess.

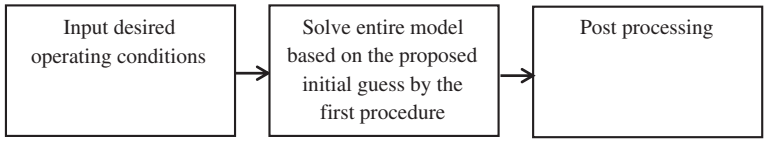

Fig. 5. Algorithm of evaluating other operating conditions.

viscous flows are considered to obtain the value of this parameter as in Eq. (26).

$$J_{mean} = \frac{\int_0^H (D_{eff} M_w \frac{dC_v}{dr} - u_{darcy}\, \rho_v) dz}{H} \quad (26)$$

In which H is the fiber length (m). Evaporation of feed is the key step in MD [49], therefore comprehensive knowledge of interfacial vapor–liquid equilibrium is essential. Two models for obtaining interfacial vapor pressure were considered in the present study; ideal solution model which is based on Raoult's law assumes activity coefficient to be one in every condition and empirical model proposed by Sparrow [46] which is based on regressed experimental data on a polynomial in a definite temperature and concentration range. The results of simulation and its comparison with corresponding experimental data are presented in Table 5. Deviation of both model's prediction results from experimental results are also computed, as presented in Table 5. As observed, empirical model generally exhibits better accuracy than ideal solution model.

Temperature polarization coefficient (TPC) is a dimensionless term that illustrates the reduction of transmembrane driving force which is caused by temperature reduction at the membrane–feed boundary [50], which can be described quantitatively by Eq. (27):

$$\mathrm{TPC} = \frac{T_m - T_{\mathrm{sat}}}{T_f - T_{\mathrm{sat}}} \quad (27)$$

where T_m, T_{sat}, and T_f are, membrane–feed temperature, corresponding saturation temperature at vacuum temperature, and bulk temperature of feed, respectively.

3.1. Effect of inlet temperature

Fig. 6(b) shows temperature distribution along the module. A surficial evaporation on shell–membrane interface causes temperature reduction along the shell side. On the other hand, in the lumen side, due to counter-current contact with the shell side, the evaporated vapor gets warmer on its way out. Fig. 6(b) reveals that most of the area in the shell side can be considered to be isothermal, except for the thin thermal boundary layer on the vicinity of membrane. This thin boundary layer is the main reason of temperature polarization phenomenon.

Increasing the temperature increases partial water vapor pressure on shell–membrane interface. Since transmembrane pressure is the main driving force in this process, increasing the inlet temperature increases the transmembrane flux [51]. Numerical representation of this phenomenon is illustrated in Fig. 7. Simulation results are in a good agreement with experimental data. Increasing the feed temperature also increases the surficial heat consumption. This has side effects on heat transfer efficiency and decreases the temperature polarization coefficient. Fig. 7 also reveals that the model which is based on Sparrow's empirical equation [46] has better agreement with experimental results compared to ideal solution model, especially at higher temperatures. For

Table 5
Comparison between experimental and simulation results of vapor flux

T_{in} (K)	P_{vac} (kPa)	$w_{0_{NaCl}}$ (%)		Ideal solution model		Empirical model	
			Experimental Flux (kg (m^2 h))	Flux (kg (m^2 h))	Error	Flux (kg (m^2 h))	Error
80	4	0.02	45.27	55.3970	0.2235	46.6584	0.0305
80	4	0.04	42.93	53.6189	0.2488	43.5774	0.0149
80	4	0.06	40.59	51.7667	0.2751	40.4999	0.0023
70	4	0.02	32.83	35.6111	0.0845	33.6193	0.0238
70	10	0.02	27.15	26.3074	0.0311	24.7749	0.0875
70	15	0.02	20.11	19.2036	0.0453	18.0295	0.1032
70	20	0.02	13.26	12.3925	0.0654	11.5619	0.1280
70	25	0.02	5.95	5.73070	0.0374	5.1820	0.1296
50	4	0.04	9.44	11.3045	0.1963	11.2230	0.1877
60	4	0.04	18.37	20.8646	0.1356	20.2146	0.1002
70	4	0.04	30.18	34.6503	0.1479	31.8640	0.0556
					Average error = 0.1355		Average error = 0.0785

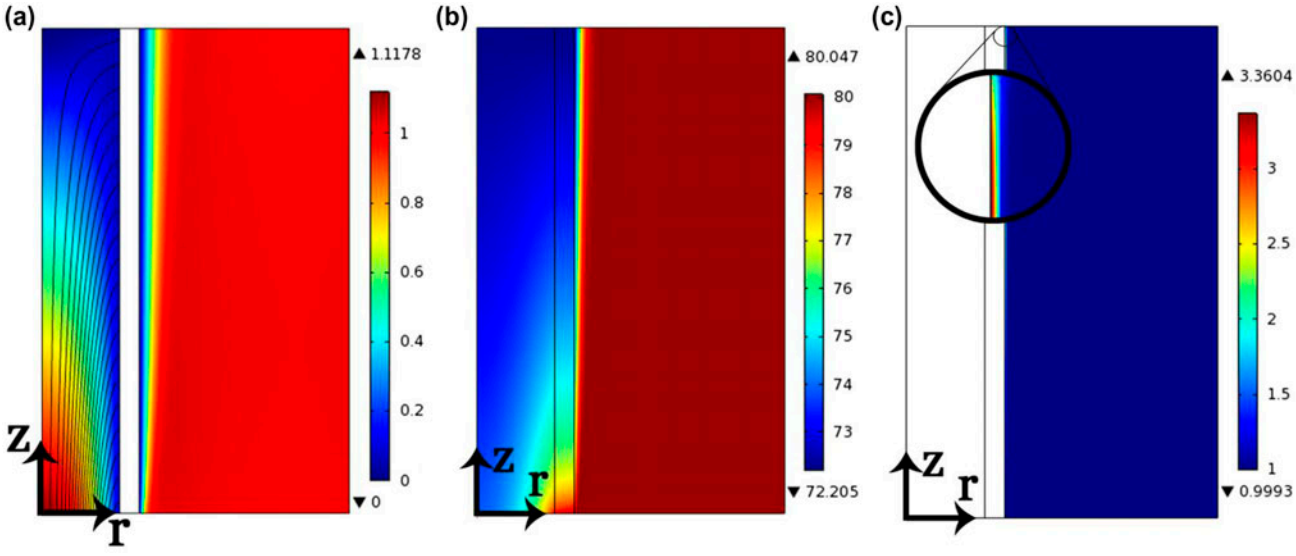

Fig. 6. (a) Velocity field and streamlines in lumen and shell sides ($V/V_{in\text{-}shell}$), (b) temperature distribution in the module (℃), (c) solute concentration distribution in the shell side (C/C_{inlet}). $T_{0,F}$ = 80 (℃); $C_{0,s}$ = 4 (wt%); $P_{perm.}$ = 4 (kPa); $Q_{0,F}$ = 20 (L/min).

describing this phenomenon, Gibbs–Duhem theorem [48] for activity coefficients (Eq. (28)) can be used to explain this phenomenon

$$x_w d\ln(\gamma_w) + x_{\mathrm{NaCl}} d\ln(\gamma_{\mathrm{NaCl}}) = 0 \quad (28)$$

which can be rewritten in the form of Eq. (29):

$$d\ln(\gamma_w) = -\frac{x_{\mathrm{NaCl}}}{x_w} d\ln(\gamma_{\mathrm{NaCl}}) \quad (29)$$

Some researchers [18,52,53] showed that increasing temperature has a direct effect on NaCl activity coefficient in aqueous solutions. Therefore, it can be concluded from Eq. (28) that increasing the temperature reduces water activity coefficient. This can describe the failure of ideal solution model at higher temperatures.

3.2. Effect of feed concentration

To achieve a better understanding ofconcentration distribution and study concentration gradient effects,

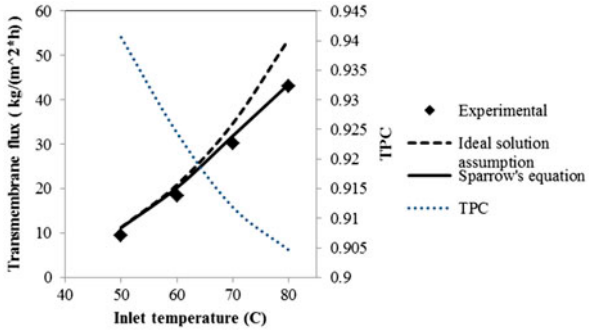

Fig. 7. Effect of feed inlet temperature on transmembrane flux and TPC. $C_{0,s} = 4$ (wt%); $P_{perm.} = 4$ (kPa); $Q_{0,F} = 20$ (L/min).

the solute concentration shouldbe calculated precisely. Fig. 6(c) shows that in a thin layer in the vicinity of membrane, a large concentration gradient is established, which has a significant effect on interfacial vapor pressure even in low inlet concentrations.

Effect of inlet salt concentration on transmembrane flux is illustrated in Fig. 8. While salt concentration increases, pure water flux slightly decreases. This reveals that increasing salt concentration reduces partial water pressure and thereby driving force of MD [51]. As it is obvious, the empirical-based model can predict much better results when compared to the ideal solution. The average slope of concentration–flux curve for the empirical-based model is more likely to be similar to experimental results. This is because of the fact that in the ideal solution model, effect of concentration on activity coefficient is not considered. The relative overestimation of ideal solution-based model cannot be totally attributed to the concentration dependency of the empirical-based model. This, based on Gibbs–Duhem theory, may be due to the fact that the ideal solution model does not have enough precision at high temperature conditions. It can also be concluded that decreasing the surficial heat consumption which is caused by concentration polarization, increases the concentration polarization coefficient.

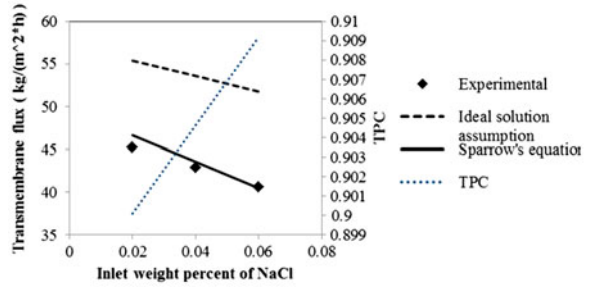

Fig. 8. Effect of inlet concentration of NaCl on transmembrane flux and TPC. $T_{0,F} = 80$ (°C); $P_{perm.} = 4$ (kPa); $Q_{0,F} = 20$ (L/min).

3.3. Effect of vacuum pressure

The use of direct vacuum can be the main difference between VMD and other MD configurations. Since the main driving force for this process is vapor pressure difference across the membrane, transmembrane flux is inversely proportional to vacuum pressure [54]. This trend might be due to the driving force reduction in MD [55]. Simulation results are compared to experimental data in Fig. 9. If the evaporation rate increases, temperature of the membrane–feed boundary decreases, and consequently the temperature polarization coefficient decreases. It can be concluded that at lower vacuum pressures, the ideal solution model tends to deviate from the experimental results. For this phenomenon, it seems that at lower vacuum pressures, when evaporation rate increases, radial velocity at the shell side in the vicinity of membrane and concentration polarization on the shell–membrane interface also increases [56]. In a reliable thermodynamic model, activity coefficient takes the effect of increasing interfacial concentration into account and the model preserves its validity even in higher concentrations; however, in the ideal solution model, since activity coefficient is always considered to be equal to unity the model is more reliable in lower concentrations.

3.4. Effect of inlet flow rate

Dimensionless velocity field in lumen and shell sides as well as streamlines in lumen side are illustrated in Fig. 6(a). Continual permeation through membrane into lumen side increases the velocity along the lumen. In order to obtain a precise knowledge about concentration and temperature polarization on

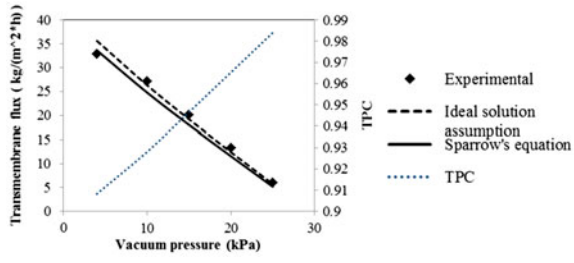

Fig. 9. Effect of vacuum pressure on transmembrane flux and TPC. $T_{0,F} = 70$ (°C) ; $C_{0,s} = 2$ (wt%); $Q_{0,F} = 20$ (L/min).

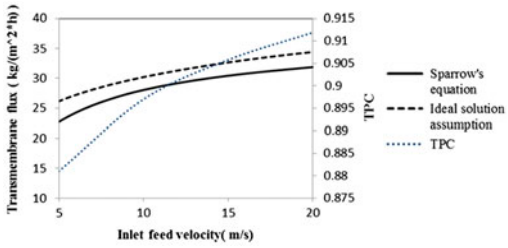

Fig. 10. Effect of inlet feed flow rate on transmembrane flux and TPC. $T_{0,F}=70$ (°C); $C_{0,s}=4$ (wt%); $P_{perm.}=4$ (kPa).

shell–membrane interface, it is essential to consider the effect of water evaporation on shell side velocity field.

It has been reported that higher feed velocities reduces boundary layer thicknesses [12,51,57], thus the extent of concentration and temperature polarizations can be reduced leading to a higher driving force between the feed and permeate sides [12]. Fig. 10 shows the effects of inlet feed velocity on transmembrane flux and polarization coefficient. It can be observed that difference between the two model predictions of transmembrane flux is higher at lower velocities. This can also be attributed to severe effect of concentration polarization at lower feed velocities.

3.5. Effect of membrane characteristics

Effects of membrane thickness, porosity, and pore diameter are illustrated in Fig. 11. Porosity and pore diameter have direct effects and membrane thickness has an inverse effect, which is consistent with Eqs. (7)–(9), (14), and (15). Fig. 11 also implies that for higher membrane transmembrane flux values, the ideal solution model deviates more from the empirical-based model and this can be attributed to the concentration polarization effects associated with higher transmembrane flux. Decreasing feed temperature at feed–membrane interface can cause TPC loss at higher transmembrane flux values.

3.6. Flux distribution in membrane

In MD, the membrane acts just as a barrier between two phases and does not have any significant effect on separation [2]. Two mass transfer mechanisms for obtaining membrane flux were considered; diffusive flux, which is driven by transmembrane chemical potential difference and viscous flow, which is driven by transmembrane pressure difference. Some researchers suggested using one mechanism and neglecting the other one based on the corresponding Knudsen's number [6,17,37], however, in some recent

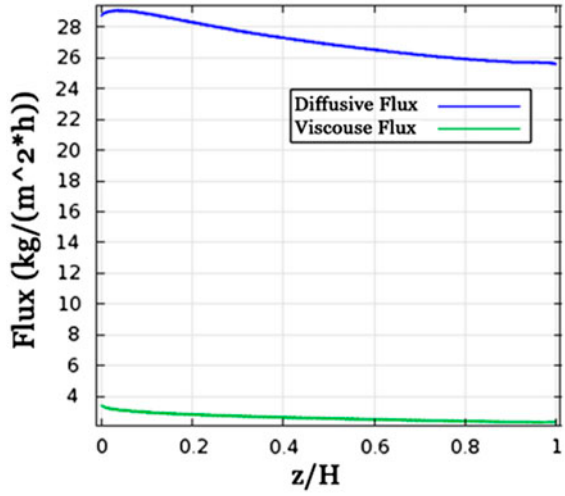

Fig. 12. Flux distribution along module. $T_{0,F}=50$ (°C); $C_{0,s}=4$ (wt%); $P_{perm.}=4$ (kPa); $Q_{0,F}=20$ (L/min).

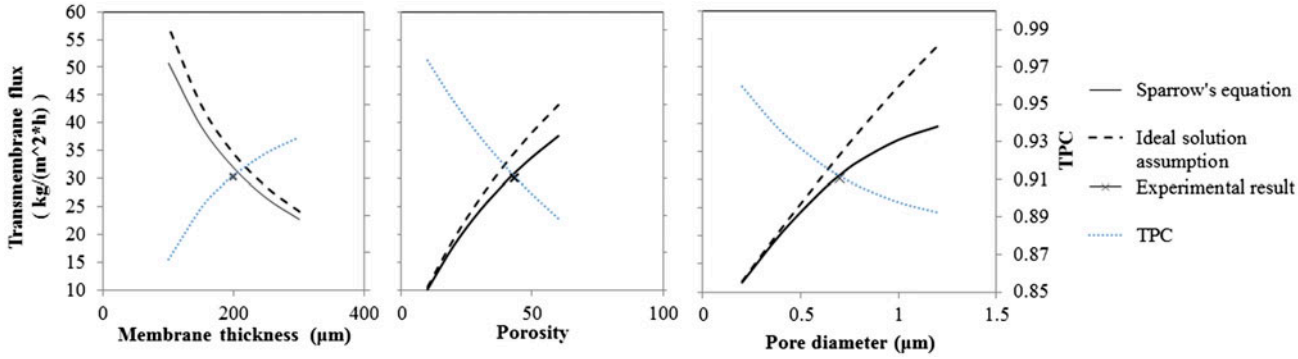

Fig. 11. Effect of membrane thickness on transmembrane flux and TPC. $T_{0,F}=70$ (°C); $C_{0,s}=4$ (wt%); $P_{perm.}=4$ (kPa); $Q_{0,F}=20$ (L/min), primary and secondary vertical axes are identical for the three plots.

articles, both mechanisms were considered [9,38,43]. The fluxes of both mechanisms vs. dimensionless module length are illustrated in Fig. 12. It can be observed that viscous flow in membrane pores which is governed by Darcy's law is less important than diffusive flux. It can be also implied from Fig. 12 that flux decreases along the module. This is because of the fact that temperature, which is the main driving force, decreases along the module [51]. Small fluctuations at the entrance of membrane can be attributed to entrance effects [58].

4. Conclusion

A numerical model based on fluid mechanics and heat and mass transfer concepts was developed. It was found out that increasing feed flow and temperature enhances transmembrane flux; however, at certain feed flow rates, the effect of feed flow rate on the VMD separation performance is much less significant. Contributions of Knudsen diffusion and free diffusion as well as viscous flow were determined by the model and it was found out that diffusion mechanism along the membrane module is more dominant compared to the viscous flow. The ideal solution model for vapor pressure prediction has been widely used in literature. A model based on ideal solution concept and another model based on an empirical equation were presented. In this study, it was observed that the two models exhibit similar predictions at low temperature conditions; however, at high temperatures and concentrations, the model based on the ideal solution concept overestimates the experimental results. The numerical method, which is based on an initial guess configuration, does speed iteration steps and reduces the probability of divergence. Also, with a small change in input parameters, the model can also be used to investigate VMD for other aqueous solutions.

Nomenclature

C	—	molar concentration, mol/m^3
D	—	diffusion coefficient, m^2/s
d	—	diameter, m
H	—	fiber height, m
J	—	volumetric flux, m/s
k	—	thermal conductivity, W/m K
l	—	membrane thickness, m
L	—	latent heat, W/kg
N	—	mass flux, $kg/m^2.s$
p	—	pressure, Pa
Q	—	flow rate, L/min
R	—	universal gas constant,$(Pa\ m^3)/(mol\ K)$
r	—	radial distance, m
T	—	temperature, K
TPC	—	temperature polarization coefficient
u	—	velocity vector in shell and lumen side
x	—	mole fraction
z	—	axial distance, m
r_1	—	inner radius of a single fiber, m
r_2	—	outer radius of a single fiber, m
r_3	—	Happel's radius, m

Greek symbols

ε	—	membrane porosity, dimensionless
κ	—	Darcian permeability, m^2
μ	—	dynamic viscosity, Pa s
ρ	—	density, kg/m^3
τ	—	membrane tortuosity, dimensionless
ϕ	—	volume fraction of void, dimensionless

Subscripts

0	—	at the inlet
eff	—	effective
knd	—	Knudsen
F	—	feed
p	—	pore
perm.	—	permeate
pol.	—	polymer
r	—	in radial direction
s	—	salt
sat.	—	in saturated condition
vac.	—	vacuum
v	—	vapor
w	—	water

References

[1] C.H. Ahn, Y. Baek, C. Lee, S.O. Kim, S. Kim, S. Lee, S.-H. Kim, S.S. Bae, J. Park, J. Yoon, Carbon nanotube-based membranes: Fabrication and application to desalination, J. Ind. Eng. Chem. (Seoul, Repub. Korea) 18 (2012) 1551–1559.

[2] F.A. Banat, F.A.A. Al-Rub, R. Jumah, M. Al-Shannag, Modeling of desalination using tubular direct contact membrane distillation modules, Sep. Sci. Technol. 34 (1999) 2191–2206.

[3] E. Close, E. Sørensen, Modelling of direct contact membrane distillation for desalination. in: S. Pierucci, G.B. Ferraris (Eds.), 20th European Symposium on Computer Aided Process Engineering. Elsevier, Naples, 2010, pp. 649–654.

[4] F. Edwie, M.M. Teoh, T.-S. Chung, Effects of additives on dual-layer hydrophobic–hydrophilic PVDF hollow fiber membranes for membrane distillation and continuous performance, Chem. Eng. Sci. 68 (2012) 567–578.

[5] A. Cipollina, M.G. Di Sparti, A. Tamburini, G. Micale, Development of a membrane distillation module for solar energy seawater desalination, Chem. Eng. Res. Des. 90 (2012) 2101–2121.

[6] H. Chang, S.-G. Lyu, C.-M. Tsai, Y.-H. Chen, T.-W. Cheng, Y.-H. Chou, Experimental and simulation study of a solar thermal driven membrane distillation desalination process, Desalination 286 (2012) 400–411.
[7] B.L. Pangarkar, M.G. Sane, S.B. Parjane, M. Guddad, Status of membrane distillation for water and wastewater treatment—A review, Desalin. Water Treat. (2013) 1–20. doi:10.1080/19443994.2013.808422.
[8] Y. Liao, R. Wang, M. Tian, C. Qiu, A.G. Fane, Fabrication of polyvinylidene fluoride (PVDF) nanofiber membranes by electro-spinning for direct contact membrane distillation, J. Membr. Sci. 425–426 (2013) 30–39.
[9] H.J. Hwang, K. He, S. Gray, J. Zhang, I.S. Moon, Direct contact membrane distillation (DCMD): Experimental study on the commercial PTFE membrane and modeling, J. Membr. Sci. 371 (2011) 90–98.
[10] S. Bandini, C. Gostoli, G.C. Sarti, Separation efficiency in vacuum membrane distillation, J. Membr. Sci. 73 (1992) 217–229.
[11] K. He, H.J. Hwang, M.W. Woo, I.S. Moon, Production of drinking water from saline water by direct contact membrane distillation (DCMD), J. Ind. Eng. Chem. (Seoul, Repub. Korea) 17 (2011) 41–48.
[12] G. Zuo, R. Wang, R. Field, A.G. Fane, Energy efficiency evaluation and economic analyses of direct contact membrane distillation system using Aspen Plus, Desalination 283 (2011) 237–244.
[13] X. Wei, B. Zhao, X.-M. Li, Z. Wang, B.-Q. He, T. He, B. Jiang, CF4 plasma surface modification of asymmetric hydrophilic polyethersulfone membranes for direct contact membrane distillation, J. Membr. Sci. 407–408 (2012) 164–175.
[14] A. Burgoyne, M.M. Vahdati, Direct contact membrane distillation, Sep. Sci. Technol. 35 (2000) 1257–1284.
[15] M.S. El-Bourawi, Z. Ding, R. Ma, M. Khayet, A framework for better understanding membrane distillation separation process, J. Membr. Sci. 285 (2006) 4–29.
[16] M.M.A. Shirazi, A. Kargari, M.J.A. Shirazi, Direct contact membrane distillation for seawater desalination, Desalin. Water Treat. 49 (2012) 368–375.
[17] T.Y. Cath, V.D. Adams, A.E. Childress, Experimental study of desalination using direct contact membrane distillation: A new approach to flux enhancement, J. Membr. Sci. 228 (2004) 5–16.
[18] E. Guillén-Burrieza, J. Blanco, G. Zaragoza, D.-C. Alarcón, P. Palenzuela, M. Ibarra, W. Gernjak, Experimental analysis of an air gap membrane distillation solar desalination pilot system, J. Membr. Sci. 379 (2011) 386–396.
[19] F. Shao, L. Ni, Y. Zhang, Y. Chen, Z. Liu, Z. Cao, Study on vacuum membrane distillation of PP hollow fiber membranes used in concentrated seawater from low-pressure reverse osmosis, Desalin. Water Treat. 51 (2013) 1–5.
[20] Z. Ji, J. Wang, D. Hou, Z. Yin, Z. Luan, Effect of microwave irradiation on vacuum membrane distillation, J. Membr. Sci. 429 (2013) 473–479.
[21] M. Khayet, P. Godino, J.I. Mengual, Theory and experiments on sweeping gas membrane distillation, J. Membr. Sci. 165 (2000) 261–272.
[22] J. Zhang, S. Gray, J.-D. Li, Modelling heat and mass transfers in DCMD using compressible membranes, J. Membr. Sci. 387–388 (2012) 7–16.
[23] J. Zhang, J.-D. Li, M. Duke, M. Hoang, Z. Xie, A. Groth, C. Tun, S. Gray, Modelling of vacuum membrane distillation, J. Membr. Sci. 434 (2013) 1–9.
[24] V. Soni, J. Abildskov, G. Jonsson, R. Gani, Modeling and analysis of vacuum membrane distillation for the recovery of volatile aroma compounds from black currant juice, J. Membr. Sci. 320 (2008) 442–455.
[25] N. Diban, O.C. Voinea, A. Urtiaga, I. Ortiz, Vacuum membrane distillation of the main pear aroma compound: Experimental study and mass transfer modeling, J. Membr. Sci. 326 (2009) 64–75.
[26] M. Coroneo, G. Montante, M. Giacinti Baschetti, A. Paglianti, CFD modelling of inorganic membrane modules for gas mixture separation, Chem. Eng. Sci. 64 (2009) 1085–1094.
[27] G. Guillen, E.M.V. Hoek, Modeling the impacts of feed spacer geometry on reverse osmosis and nanofiltration processes, Chem. Eng. J. 149 (2009) 221–231.
[28] E. Kougoulos, A.G. Jones, M. Wood-Kaczmar, CFD modelling of mixing and heat transfer in batch cooling crystallizers, Chem. Eng. Res. Des. 83 (2005) 30–39.
[29] S.X. Liu, M. Peng, L. Vane, CFD modeling of pervaporative mass transfer in the boundary layer, Chem. Eng. Sci. 59 (2004) 5853–5857.
[30] S. Wardeh, H.P. Morvan, CFD simulations of flow and concentration polarization in spacer-filled channels for application to water desalination, Chem. Eng. Res. Des. 86 (2008) 1107–1116.
[31] R.J. Byron Smith, L. Muruganandam, S. Murthy Shekhar, CFD analysis of water gas shift membrane reactor, Chem. Eng. Res. Des. 89 (2011) 2448–2456.
[32] S. Ahmed, M.T. Seraji, J. Jahedi, M.A. Hashib, Application of CFD for simulation of a baffled tubular membrane, Chem. Eng. Res. Des. 90 (2012) 600–608.
[33] X. Yang, H. Yu, R. Wang, A.G. Fane, Analysis of the effect of turbulence promoters in hollow fiber membrane distillation modules by computational fluid dynamic (CFD) simulations, J. Membr. Sci. 415–416 (2012) 758–769.
[34] M. Shakaib, S.M.F. Hasani, I. Ahmed, R.M. Yunus, A CFD study on the effect of spacer orientation on temperature polarization in membrane distillation modules, Desalination 284 (2012) 332–340.
[35] H. Yu, X. Yang, R. Wang, A.G. Fane, Analysis of heat and mass transfer by CFD for performance enhancement in direct contact membrane distillation, J. Membr. Sci. 405–406 (2012) 38–47.
[36] H. Yu, X. Yang, R. Wang, A.G. Fane, Numerical simulation of heat and mass transfer in direct membrane distillation in a hollow fiber module with laminar flow, J. Membr. Sci. 384 (2011) 107–116.
[37] N. Tang, H. Zhang, W. Wang, Computational fluid dynamics numerical simulation of vacuum membrane distillation for aqueous NaCl solution, Desalination 274 (2011) 120–129.
[38] M. Ghadiri, S. Fakhri, S. Shirazian, Modeling and CFD simulation of water desalination using nanoporous membrane contactors, Ind. Eng. Chem. Res. 52 (2013) 3490–3498.
[39] H. Fang, J.F. Gao, H.T. Wang, C.S. Chen, Hydrophobic porous alumina hollow fiber for water desalination via membrane distillation process, J. Membr. Sci. 403–404 (2012) 41–46.

[40] J. Happel, Viscous flow relative to arrays of cylinders, AIChE J. 5 (1959) 174–177.
[41] M. Khayet, Membranes and theoretical modeling of membrane distillation: A review, Adv. Colloid Interface Sci. 164 (2011) 56–88.
[42] R.E. Treybal, Mass-Transfer Operations, 3rd ed., McGraw-Hill, Burr Ridge, IL, 1980.
[43] F. Chen, R. Mourhatch, T.T. Tsotsis, M. Sahimi, Pore network model of transport and separation of binary gas mixtures in nanoporous membranes, J. Membr. Sci. 315 (2008) 48–57.
[44] R.H. Perry, D.W. Green, Perry's Chemical Engineers' Handbook, McGraw Hill, New York, NY, 1997.
[45] R.W. Baker, Membrane Technology and Applications, John Wiley & Sons, San Francisco, CA, 2004.
[46] B.S. Sparrow, Empirical equations for the thermodynamic properties of aqueous sodium chloride, Desalination 159 (2003) 161–170.
[47] K.W. Lawson, D.R. Lloyd, Review Membrane distillation, J. Membr. Sci. 124 (1997) 1–25.
[48] J. Smith, H. Van Ness, M. Abbott, Chemical Engineering Thermodynamics, McGraw-Hill, Boston, MA, 2001.
[49] L. Martínez-Díez, F.J. Florido-Díaz, M.I. Vázquez-González, Study of evaporation efficiency in membrane distillation, Desalination 126 (1999) 193–198.
[50] M. Khayet, T. Matsuura, Pervaporation and vacuum membrane distillation processes: Modeling and experiments, AIChE J. 50 (2004) 1697–1712.
[51] F.A. Banat, F.A. Al-Rub, M. Shannag, Modeling of dilute ethanol–water mixture separation by membrane distillation, Sep. Purif. Technol. 16 (1999) 119–131.
[52] M.L. Brendel, S.I. Sandler, The effect of salt and temperature on the infinite dilution activity coefficients of volatile organic chemicals in water, Fluid Phase Equilib. 165 (1999) 87–97.
[53] C. Berg, A.C. McKinnis, Effect of temperature on liquid phase activity coefficients, Ind. Eng. Chem. 40 (1948) 1309–1311.
[54] J. Zhang, J.-D. Li, M. Duke, Z. Xie, S. Gray, Performance of asymmetric hollow fibre membranes in membrane distillation under various configurations and vacuum enhancement, J. Membr. Sci. 362 (2010) 517–528.
[55] S.G. Lovineh, M. Asghari, B. Rajaei, Numerical simulation and theoretical study on simultaneous effects of operating parameters in vacuum membrane distillation, Desalination 314 (2013) 59–66.
[56] M. Mulder, Basic Principles of Membrane Technology, 2nd ed., Kluwer Academic Pub., Dordrecht, 1996.
[57] A. Bahmanyar, M. Asghari, N. Khoobi, Numerical simulation and theoretical study on simultaneously effects of operating parameters in direct contact membrane distillation, Chem. Eng. Process. 61 (2012) 42–50.
[58] C. Rodrigues, V. Geraldes, M.N. de Pinho, V. Semião, Mass-transfer entrance effects in narrow rectangular channels with ribbed walls or mesh-type spacers, Chem. Eng. Sci. 78 (2012) 38–45.